
CMS Physics Analysis Summary

Contact: cms-pag-conveners-bphysics@cern.ch

2020/06/11

Measurement of prompt open-charm production cross sections in proton-proton collisions at $\sqrt{s} = 13$ TeV

The CMS Collaboration

Abstract

The production cross section for prompt open-charm mesons is measured in proton-proton collisions at the LHC center-of-mass energy of 13 TeV. The data sample corresponds to an integrated luminosity of 29 nb^{-1} collected by the CMS experiment in 2016. The differential cross sections of the $D^{*\pm}$, D^\pm , and $D^0(\bar{D}^0)$ mesons are presented in bins of transverse momentum and pseudorapidity in the range $4 < p_T < 100$ GeV and $|\eta| < 2.1$, respectively. The results are also compared to several theoretical calculations and to previous measurements.

1 Introduction

Measurements of the production cross section for charm mesons in hadronic collisions at high center-of-mass energies provide an important test of strong interactions, referred to as quantum chromodynamics (QCD). Furthermore, since the current calculations suffer from large theoretical uncertainties, experimental constraints on heavy-quark production cross sections are relevant for all the physics phenomena for which heavy-quark production is an important background process. Several studies have been carried out at the LHC at $\sqrt{s} = 7$ TeV by the ALICE [1] and ATLAS [2] Collaborations, while the LHCb Collaboration has published results at $\sqrt{s} = 5$ [3], 7 [4], and 13 TeV [5]. The CMS experiment has produced results on open-charm production, analyzing heavy-ion and proton-proton (pp) collisions at $\sqrt{s} = 5.02$ TeV [6], but no results have yet been published on pp collisions at $\sqrt{s} = 13$ TeV. The new measurements presented in this paper cover kinematic regions different from those used earlier. Hence, the results from this paper contribute to a deeper understanding of the charm meson production mechanism.

Charm mesons arising from the pp collision point, either directly or as decay products of excited charm resonances (e.g., D^0 (and \bar{D}^0) coming from $D^{*\pm}$ decay), are referred to as promptly produced, while charm mesons coming from the decays of b mesons, i.e., $B \rightarrow DX$ where X is any additional final state, are referred to as secondary charm (thus nonprompt) and are considered as a background process. This analysis is focused on the measurement of the cross section for the prompt production of $D^{*\pm}$, D^0 (and \bar{D}^0), and D^\pm (noted below as D^{*+} , D^0 , and D^+). The analyzed data was collected by the CMS experiment in 2016 pp collisions at $\sqrt{s} = 13$ TeV.

In this paper the study of charm meson decays proceeds through the exclusive channels:

- $pp \rightarrow D^{*+} X \rightarrow D^0 \pi_s^+ X \rightarrow K^- \pi^+ \pi_s^+ X$,
- $pp \rightarrow D^0 X \rightarrow K^- \pi^+ X$,
- $pp \rightarrow D^+ X \rightarrow K^- \pi^+ \pi^+ X$,

where charge conjugation is implied here and throughout this paper, if not specified. The designation π_s indicates that, because of the specific kinematics of the $D^{*\pm}$ decay, this slow pion has significantly lower momentum than the kaon and pion decay products of the D^0 .

The single differential cross sections for the charm mesons as a function of the transverse momentum p_T and the pseudorapidity $|\eta|$ are measured. The measured cross sections are compared to PYTHIA [7, 8], POWHEG [9], and FONLL [10] calculations and to the other LHC results.

2 Data, simulation and event selection

The data sample used in this analysis was collected with the CMS detector at the LHC in 2016, in pp collisions at a center-of-mass energy of 13 TeV, and corresponds to an integrated luminosity of 29 nb^{-1} , out of the 36.8 fb^{-1} collected in the 2016 data-taking period. The average number of simultaneous pp collisions in the same or nearby bunch crossings, pileup (PU), for the subset of data used for this analysis is 14.

A simulated signal sample is used to measure the efficiency and the acceptance, and to parameterize the kinematic variable distributions of the data for all three charm mesons. Event samples using Monte Carlo (MC) simulations are generated with PYTHIA 6.4 [7] and processed by the simulation framework of the CMS detector based on GEANT4 v10.00.p02 [11]. The decays $D^{*+} \rightarrow D^0 \pi_s^+ \rightarrow K^- \pi^+ \pi_s^+$, in which the signal sample is enriched, are modeled with the VSS model of EVTGEN 1.3.0 [12]. Although the filter selects only the D^{*+} decay, the sample

is used for all the three channels because of the large available statistics. A small filter bias for the D^+ p_T distribution has been corrected by reweighting the simulated sample for the D^+ final state according to the D^{*+} p_T shape.

To avoid any possible bias in the selection, data events were collected with an inclusive trigger that only required the presence of colliding beams. The physics objects reconstructed in the final states have low enough p_T values for additional trigger requirements to have a nonnegligible effect on their selection. The efficiency of the inclusive trigger is 100%. The candidate vertex with the largest value of summed physics-object p_T^2 is taken to be the primary pp interaction vertex (PV). The physics objects are the jets, clustered using the jet-finding algorithm [13, 14] with the tracks assigned to candidate vertices as inputs, and the associated missing transverse momentum, taken as the negative vector sum of the \vec{p}_T of those jets. The efficiency of the signal events for this selection has a dependence on p_T and $|\eta|$ of the reconstructed charm meson. In order to ensure a correct calculation of the total reconstruction efficiency, a pileup reweighting is performed in the simulated sample to reproduce the distribution in data.

3 Analysis Strategy

3.1 Charm meson reconstruction

The D^{*+} , D^0 , and D^+ charm mesons are reconstructed in the range of transverse momentum $4 < p_T(D) < 100$ GeV and pseudorapidity $|\eta(D)| < 2.1$, where D represents D^{*+} , D^0 , and D^+ .

The first step in the reconstruction of the charm mesons is the selection of the tracks corresponding to the objects in the final states. The kaon and pion tracks are required to satisfy the following criteria: $p_T > 0.5$ GeV; reduced track fit $\chi^2 < 2.5$; number of hits in the strip plus pixel layers ≥ 5 ; number of hits in the pixel subdetector only ≥ 2 ; an impact parameter in the transverse plane (IP_{xy}) w.r.t. the PV < 0.1 cm; an impact parameter in the z direction (IP_z) with respect to the PV < 1 cm.

For the reconstruction of the D^{*+} decay chain, the additional slow pion track produced in association with the D^0 is selected with more relaxed conditions. Such a track is required to have $p_T > 0.3$ GeV, $\chi^2/\text{dof} < 3$ where dof is the number of degrees of freedom, and the total number of hits in the tracker > 2 . The significance of the impact parameters in the x-y plane and in the z direction with respect to the PV, defined as the ratio between the impact parameter value and its uncertainty, is required to be less than 3.

The approach in the meson reconstruction is very similar for all the three mesons, because of the common features among them. The general strategy is as follows: charm mesons are reconstructed by combining two (three) tracks with total charge 0 (1) for the D^0 (D^+) candidates, having an invariant mass within a specific range around the nominal mass of the mesons. In the p_T range relevant for this analysis, charged pions, kaons, and protons cannot be separated efficiently in the CMS detector. A kaon or pion mass hypothesis is thus assumed for the tracks, according to the charge and the specific decay channel. For the neutral D^0 meson, the contribution of the wrong mass assignment (i.e., K- π swapped) is studied in the simulated sample and will be described in the next section. The two- or three-track combinations must be compatible with having a common secondary vertex (SV) with a vertex fit χ^2 probability greater than 1%. The cosine of the angle between the charm candidate momentum and the vector pointing from the PV to the SV in the transverse plane ($\cos\phi$) must be greater than 0.99, thus requiring the D^0 or D^+ meson to be consistent with originating from the PV. This requirement greatly reduces the contribution from b hadron decays.

A selection requirement, specific to each meson, on the significance in the transverse decay length L , defined as the distance between the SV and PV in the transverse plane, divided by its uncertainty, is also set. This is a crucial requirement in the analysis since it refers to the specific topology of the decays and provides a considerable reduction in the combinatorial background.

To complete the D^{*+} meson reconstruction, an additional third track with the looser selection, corresponding to the slow pion, is kinematically combined with the D^0 candidate. Since there can be more than one candidate per event, an arbitration criterion for the final selection is used and the combination with an invariant mass closest to the nominal one ($M^{\text{PDG}}(D)$) [15] is kept for the D^0 and D^+ candidates, while for the D^{*+} the one with the lowest mass difference $\Delta M = M(K\pi\pi_s) - M(K\pi)$ is chosen. Arbitration for charge conjugate final states is treated separately. It was checked that this criterion does not introduce a statistically significant bias in terms of either signal yield or invariant mass distribution by comparing this method with a random selection of candidates.

This general strategy is then optimized for each of the reconstructed charm mesons, with the specific requirements reported in Table 1. The largest contribution to the background comes from random combinatorial candidates. The tight selection criteria greatly reduces this contribution in favor of the signal events.

Table 1: The values of the selection requirements for each charm meson.

Variables	D^{*+}	D^0	D^+
PV selection:	largest $\sum p_T^2$	largest $\sum p_T^2$	largest $\sum p_T^2$
Tracks: p_T^{\min} [GeV]	0.5 (0.3 for the π_s)	0.8	0.7
Tracks: reduced χ^2	< 2.5 (3 for the π_s)	< 2.5	< 2.5
Tracks: N Tracker Hits	≥ 5 (> 2 for the π_s)	≥ 5	≥ 5
Tracks: N Pixel Hits	≥ 2 (none for the π_s)	≥ 2	≥ 2
Tracks: IP_{xy} [cm]	< 0.1 (sig. < 3 for π_s)	< 0.1	< 0.1
Tracks: IP_z [cm]	< 1 (sig. < 3 for π_s)	< 1	< 1
$ M_{\text{cand}} - M^{\text{PDG}} $ [GeV]	< 0.023	< 0.10	< 0.10
SV fit CL	> 1%	> 1%	> 1%
Pointing, $\cos\Phi$	> 0.99	> 0.99	> 0.99
L significance:	> 3	> 5	> 10
Arbitration	min ΔM	min $ M(K\pi) - M^{\text{PDG}}(D^0) $	min $ M(K\pi\pi) - M^{\text{PDG}}(D^+) $

3.2 Signal yield determination

The charm meson differential cross section $d\sigma/dp_T$ is measured in 9 bins of p_T between 4 and 100 GeV in the pseudorapidity range $|\eta| < 2.1$; the differential cross section $d\sigma/d|\eta|$ is measured in 10 bins of $|\eta|$ for p_T between 4–100 GeV.

The signal yields are determined using unbinned maximum-likelihood fits to the invariant mass distributions for the various decay modes (the ΔM distribution is considered for the D^{*+}) in each p_T and $|\eta|$ bin. The signal components are modeled by the sum of two Gaussian functions to account for the nonuniform resolution over the detector, keeping the mean, the width, and the normalization term as free parameters. An additional Gaussian function is used to describe the invariant mass shape of D^0 candidates with the incorrect pion and kaon mass assignments. The width of this wide Gaussian is taken bin-by-bin from simulation. The normalization of the wide Gaussian contribution is fixed to be the same as that of the sum of the two narrow Gaussians in each bin, reflecting the fact that the number of correct and swapped

Table 2: The signal yields in data and the statistical uncertainties for D^{*+} , D^0 , and D^+ mesons in p_T bins for $|\eta| < 2.1$.

p_T range [GeV]	D^{*+} Yield	D^0 Yield	D^+ Yield
4–5	901 ± 40	5200 ± 700	5850 ± 1400
5–6	1555 ± 99	5480 ± 400	3390 ± 460
6–7	1450 ± 98	5640 ± 450	3620 ± 140
7–8	1144 ± 75	3990 ± 500	2790 ± 130
8–12	2962 ± 80	9750 ± 320	6860 ± 180
12–16	1170 ± 120	3540 ± 170	3047 ± 96
16–24	647 ± 28	2040 ± 120	1821 ± 77
24–40	180 ± 15	625 ± 58	628 ± 61
40–100	38 ± 6	91 ± 20	83 ± 11

Table 3: The signal yields in data and the statistical uncertainties for D^{*+} , D^0 , and D^+ mesons with $4 < p_T < 100$ GeV in η bins.

$ \eta $ range	D^{*+} Yield	D^0 Yield	D^+ Yield
0–0.2	1227 ± 42	3640 ± 120	3200 ± 110
0.2–0.4	1340 ± 150	4150 ± 140	3060 ± 96
0.4–0.6	1276 ± 45	4280 ± 150	2910 ± 190
0.6–0.8	1540 ± 110	4590 ± 180	3200 ± 230
0.8–1	1283 ± 68	3700 ± 210	3040 ± 140
1–1.2	1026 ± 88	4270 ± 320	3180 ± 160
1.2–1.4	860 ± 110	3180 ± 300	2850 ± 160
1.4–1.6	580 ± 190	3050 ± 320	2350 ± 250
1.6–1.8	530 ± 84	2200 ± 510	2130 ± 210
1.8–2.1	539 ± 69	3770 ± 590	2780 ± 490

K/π candidate associations for the D^0 signal is the same by definition.

The combinatorial background is described with different functions, according to the decay mode. For the D^{*+} meson the background is described by a phenomenological threshold function [16] given by

$$f = \left(1 - e^{-\frac{\Delta M - M_0}{p_0}}\right) \left(\frac{\Delta M}{M_0}\right)^{p_1} + p_2 \left(\frac{\Delta M}{M_0} - 1\right), \quad (1)$$

where M_0 is the endpoint, taken to be the pion mass, and $p_{0,1,2}$ are free parameters. For the D^0 and D^+ mesons the combinatorial background component is modeled by a third-degree polynomial function, where the four coefficients are free parameters. The signal yields and the statistical uncertainties returned by the fits are reported in Tables 2 and 3 for the p_T and $|\eta|$ bins, respectively.

In Fig. 1 the fitted invariant mass distributions are reported in two of the p_T bins, low (5–6 GeV) and high (16–24 GeV); while in Fig. 2 the fitted invariant mass distributions are shown for the bins $|\eta| < 0.2$ and $1.6 < |\eta| < 1.8$. As expected, at low p_T and high $|\eta|$ the resolution of the detector is worse, which affects the mass width and the distribution shapes, with a consequent increase in the combinatorial background. Despite the different kinematic regions, it was found that the same functions reproduce all the distributions well.

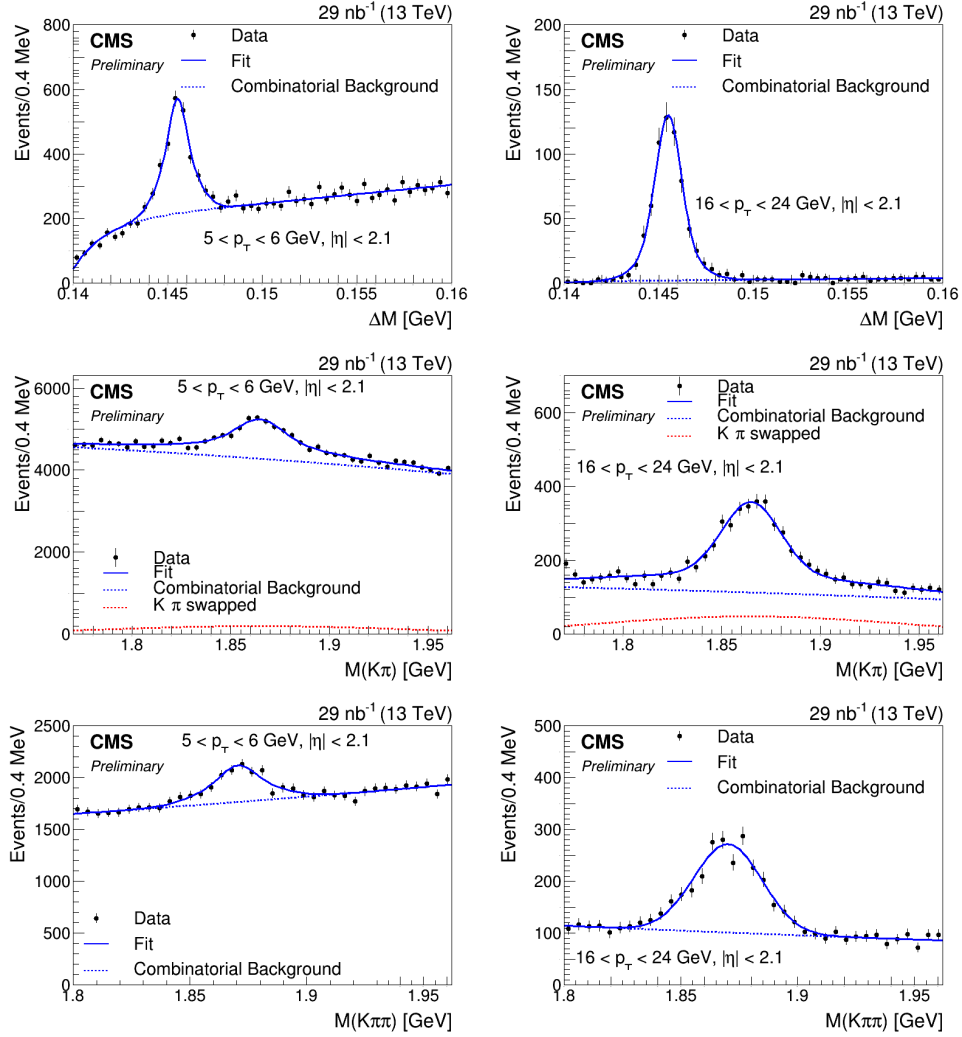


Figure 1: Mass distributions for: $K^- \pi^+ \pi^+ - K^- \pi^+$ (upper), $K^- \pi^+$ (middle), and $K^- \pi^+ \pi^+$ (lower); charged conjugation is implied. Figures in the left column show the p_T bin 5–6 GeV, while the 16–24 GeV p_T bin is shown on the right.

3.3 Efficiency measurement

The efficiency is measured on a large simulated signal sample. It is defined as the fraction of simulated charm decays, generated in the kinematic region $4 < p_T < 100 \text{ GeV}$ and $|\eta| < 2.1$, that survives the selection criteria described in Section 3.1. The efficiency is thus calculated for each p_T and $|\eta|$ bin and for both the charged states. Taking the D^{*+} channel as an example, these values range from 0.6% for $4 < p_T < 5 \text{ GeV}$ to 30% for $40 < p_T < 100 \text{ GeV}$, and from 3.8% for $|\eta| < 0.2$ to 1.5% for $1.8 < |\eta| < 2.1$.

3.4 Contamination from secondary decay

The aim of this work is to measure the prompt open-charm production cross sections. Thus, it is important to evaluate and subtract the contribution coming from nonprompt charm mesons arising from b hadron decays. Since consistency with the PV is already part of the selection requirements, the prompt signals and secondary-decay components have similar kinematic variable distributions. The contamination rate is quantified using a simulation-based strategy. Using the information from the event generators, two subsamples are identified to be repre-

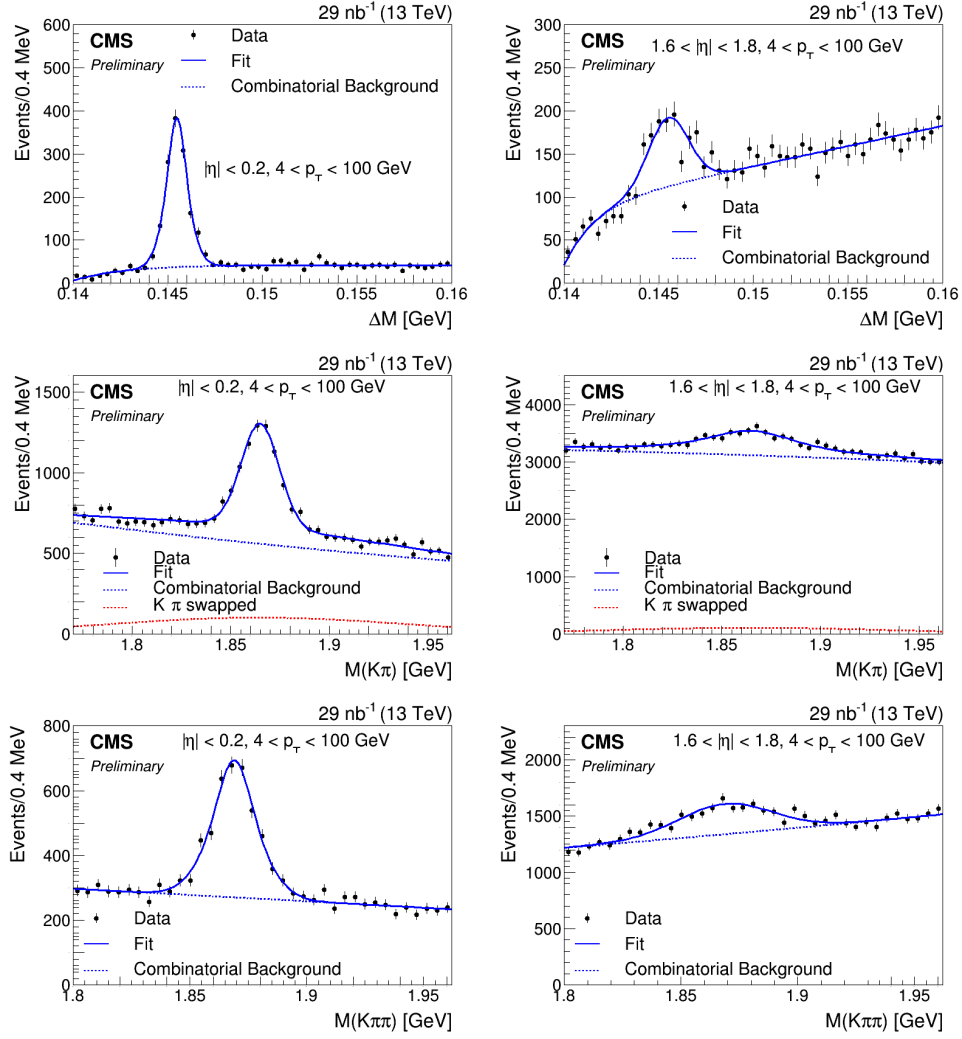


Figure 2: Mass distributions for: $K^- \pi^+ \pi^+_{\text{s}} - K^- \pi^+$ (upper), $K^- \pi^+$ (middle), and $K^- \pi^+ \pi^+$ (lower); charged conjugation is implied. Figures in the left column show the $|\eta| < 0.2$ bin, while the $1.6 < |\eta| < 1.8$ bin is shown on the right.

sentative of prompt charm mesons and nonprompt contributions. The same reconstruction strategy described in Section 3.1 is applied to both of them and the yields N_{prompt} and N_{sec} are computed, as reported in Section 3.2. The contamination is then evaluated as the ratio of N_{sec} to the sum ($N_{\text{prompt}} + N_{\text{sec}}$) for each p_T and $|\eta|$ bin. The contamination is nonnegligible, ranging from 5 to 17%, in any of the p_T and $|\eta|$ bins and for any reconstructed meson. This is expected, because the requirement on the lifetime significance to reject combinatorial backgrounds tends to select long-lived mesons. In Fig. 3 the contamination rates for the three mesons are reported as a function of p_T (left) and $|\eta|$ (right) bins, respectively.

The nonprompt component of the signal is evaluated based on results from simulations, after ensuring a good kinematic description of data events. The contamination rate obtained with this method is subtracted from the measured values of the visible cross section for each p_T and $|\eta|$ bin.

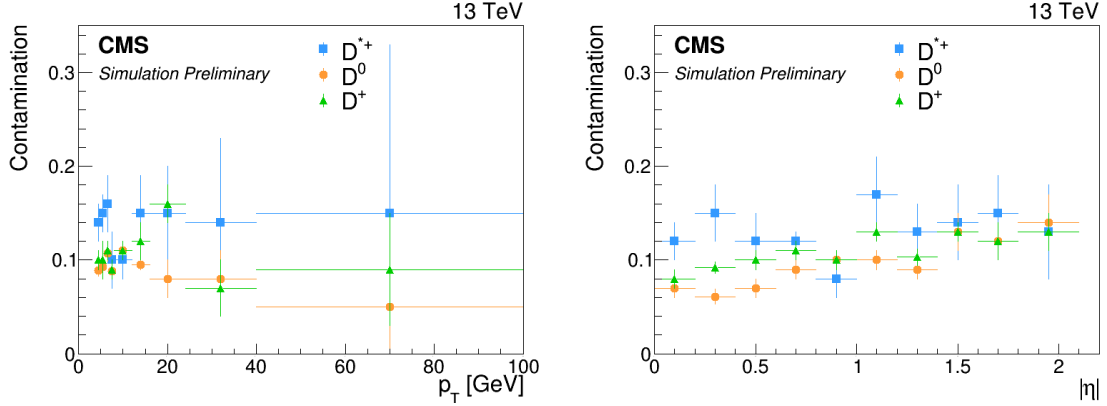


Figure 3: Contamination from secondary decay reported as a function of p_T (left) and $|\eta|$ (right) for D^{*+} (square), D^0 (circle), and D^+ (triangle) mesons. The vertical lines represent the statistical uncertainties.

4 Systematic uncertainties

Several systematic uncertainty sources are considered in the measurement of the charm meson cross sections. The dominant effects come from the uncertainty related to the tracking efficiency and the mass distribution modeling used in the fit for both signal and background components. All the uncertainties considered in this analysis can be organized into three different categories: decay mode and bin dependent, only decay mode dependent, and independent of both decay mode and bin.

The first category includes the limited amount of events in the MC simulation sample used for the efficiency calculation, resulting in a systematic uncertainty of 0.3, 0.3, and 3.5%, respectively, for the D^{*+} , D^0 , and D^+ mesons. The last uncertainty is larger than the other two since the sample was enriched in $D^{*+} \rightarrow D^0 \pi^+ \pi_s^- \rightarrow K^- \pi^+ \pi_s^+$. The uncertainties in the nonprompt event contamination were treated similarly. The resulting systematic uncertainties are: 2.9% for the D^{*+} , 0.8% for the D^0 , and 1.4% for the D^+ .

The limited number of background events peaking in the signal region because of the invariant mass arbitration requirement also contributes to the first uncertainty category. This was studied in simulated sample events by selecting a control region that does not contain events with charm mesons. It was found to have a nonnegligible contribution only for the D^+ meson. The effect for the D^+ was evaluated in each bin and found to contribute a systematic uncertainty of 8% for $p_T < 12$ GeV, but to be negligible at higher p_T values. This contribution is independent of η , and an uncertainty of 6% is determined for all $|\eta|$ bins. This is considered as part of the background modeling systematic uncertainty.

Another source of systematic uncertainty that is included in this category comes from the p_T selection criterion applied to the π_s in the D^{*+} decay chain. The p_T spectrum of the slow pion peaks below 0.5 GeV and the selection requirement of $p_T > 0.3$ GeV affects the reconstruction efficiency in the first p_T bin (4–5 GeV). A systematic uncertainty of 9% is assigned for this bin, which reflects the variation of the simulated event efficiency calculation in the two bins $200 < p_T(\pi_s) < 300$ MeV and $300 < p_T(\pi_s) < 400$ MeV.

Since a reweighting is applied to the MC simulated events in order to reproduce the data PU distribution, a systematic uncertainty is evaluated for each final state. The statistical uncertainty related to the weight $w = \text{data}/\text{MC}$ is calculated for each bin. The cross sections are then reevaluated using the weights raised and lowered by their statistical uncertainties. The

largest bin-by-bin change with respect to the cross section calculated with the central value of the weight is taken as the corresponding systematic uncertainty. The total effect is 1% for D^{*+} and D^0 and 2% for the D^+ . The systematic uncertainty due to the selection requirement on the significance of the transverse decay distance L was studied and found to be small compared to other sources.

The uncertainties associated with the branching fraction values and the track reconstruction efficiency depend on the decay mode but not on p_T or η . The first one is taken from Ref. [15] and has values of 1.1, 0.8, and 1.7% for D^{*+} , D^0 , and D^+ . An uncertainty is assigned to the track reconstruction efficiency according to [17]. A different consideration is needed for the slow pion in the D^{*+} decay. Because of the soft p_T spectrum a lower tracking efficiency is expected. The uncertainty related to the slow pion is computed by comparing the yield in data and MC simulated events when varying the p_T and η of the slow pion. This results in a systematic uncertainty of 5.2%. Combining the uncertainties for each track, the total systematic uncertainty from this source is 9.4, 4.2, and 6.1% for the D^{*+} , D^0 , and D^+ , respectively.

The systematic uncertainty due to the modeling of the invariant mass distribution also falls into the second category. As described in Section 3.2, the signal yields are computed by modeling the resonance peaks with a double-Gaussian function in order to take into account the different resolution effects in various kinematic regions. The uncertainty is estimated by using instead a single Gaussian function, the sum of three Gaussian functions, or a Crystal Ball function [18, 19]. The largest deviation with respect to the baseline function is then taken as systematic uncertainty, giving 3.6, 5.0, and 4.2% for the D^{*+} , D^0 , and D^+ . For the combinatorial background description the systematic uncertainty is evaluated by replacing the baseline function with a fourth-degree polynomial, resulting in 1.2% for the D^{*+} , 4.8% for the D^0 , and 5.3% for the D^+ .

The last category, containing uncertainties independent of both decay modes and kinematic variables, includes those due to data-taking conditions and detector performances. The systematic uncertainty in the integrated luminosity for 2016 is 2.5% [20]. During the 2016 run, the CMS tracker suffered some time-dependent inefficiencies that resulted in a nonnegligible change in charm meson yields. The average PU rate also varied during the data taking. Both these effects are taken into account by correcting the different runs for the tracker inefficiency, which was determined from simulation after the PU distribution in the simulated events was reweighted to match the data. The resulting systematic uncertainty in the correction is estimated to be 1.4%.

All the systematic uncertainties are summarized in Table 4. The total uncertainty is evaluated as the sum in quadrature of the individual contributions.

5 Results

The differential cross sections for prompt charm meson production as a function of p_T and $|\eta|$ are determined using the equations:

$$\frac{d\sigma(pp \rightarrow DX)}{dp_T} = \frac{N_i(D \rightarrow f)}{\Delta p_T \mathcal{B}(D \rightarrow f) \mathcal{L} \varepsilon_{i,tot}(D \rightarrow f)}, \quad (2)$$

$$\frac{d\sigma(pp \rightarrow DX)}{d|\eta|} = \frac{N_i(D \rightarrow f)}{\Delta \eta \mathcal{B}(D \rightarrow f) \mathcal{L} \varepsilon_{i,tot}(D \rightarrow f)}, \quad (3)$$

where $N_i(D \rightarrow f)$ is the number of prompt charm meson reconstructed in the selected final

Table 4: Summary of the systematic uncertainties in the D^{*+} , D^0 , and D^+ cross sections. The total uncertainty is the sum in quadrature of the individual contributions.

	Relative uncertainties (%)		
	D^{*+}	D^0	D^+
Signal efficiency calculation	0.3	0.3	3.5
Secondary decay contamination	2.9	0.8	1.4
PU reweighting	1.0	1.0	2.0
Branching fraction	1.1	0.8	1.7
Tracking efficiency	9.4	4.2	6.1
Signal modeling	3.6	5.0	4.2
Background modeling	1.2	4.8	8.0
Luminosity	2.5	2.5	2.5
Time-dependent inefficiencies	1.4	1.4	1.4
Total	11.0	8.7	12.2

state (including the charge conjugate final state) for each bin i , after correcting for contamination, Δp_T and $\Delta\eta = 2\Delta|\eta|$ are the p_T and $|\eta|$ bin widths, respectively, $\mathcal{B}(D \rightarrow f)$ is the branching fraction of the reconstructed final state, $\varepsilon_{i,tot}(D \rightarrow f)$ is the total reconstruction efficiency of the decay chain evaluated in the simulated events sample, and \mathcal{L} is the collected luminosity.

In Tables 5 and 6 the differential cross section values are reported for each p_T and $|\eta|$ bin, respectively. The central values are reported with their uncertainties: the first one is the statistical and the second one the systematic uncertainty.

Table 5: The differential cross sections of $D^{*\pm}$, D^0 (\bar{D}^0), and D^\pm in p_T bins with $|\eta| < 2.1$; the first uncertainty is statistical, the second is systematic.

p_T bin [GeV]	$D^{*\pm} d\sigma/dp_T (\mu\text{b}/\text{GeV})$	$D^0 (\bar{D}^0) d\sigma/dp_T (\mu\text{b}/\text{GeV})$	$D^\pm d\sigma/dp_T (\mu\text{b}/\text{GeV})$
4–5	$166 \pm 7 \pm 23$	$430 \pm 58 \pm 38$	$250 \pm 61 \pm 33$
5–6	$96 \pm 6 \pm 10$	$230 \pm 17 \pm 21$	$79 \pm 11 \pm 11$
6–7	$47 \pm 3 \pm 5$	$136 \pm 11 \pm 12$	$50 \pm 2 \pm 7$
7–8	$25.6 \pm 1.7 \pm 2.8$	$66 \pm 8 \pm 6$	$29.5 \pm 1.4 \pm 4.2$
8–12	$8.8 \pm 0.2 \pm 1.0$	$21.0 \pm 0.7 \pm 1.9$	$9.4 \pm 0.3 \pm 1.2$
12–16	$1.70 \pm 0.17 \pm 0.19$	$3.93 \pm 0.19 \pm 0.44$	$2.05 \pm 0.07 \pm 0.24$
16–24	$(3.52 \pm 0.15 \pm 0.42) \times 10^{-1}$	$(8.1 \pm 0.5 \pm 0.9) \times 10^{-1}$	$(4.06 \pm 0.17 \pm 0.51) \times 10^{-1}$
24–40	$(4.1 \pm 0.3 \pm 0.6) \times 10^{-2}$	$(9.7 \pm 0.9 \pm 1.3) \times 10^{-2}$	$(6.0 \pm 0.6 \pm 1.0) \times 10^{-2}$
40–100	$(2.3 \pm 0.4 \pm 0.5) \times 10^{-3}$	$(3.3 \pm 0.7 \pm 0.8) \times 10^{-3}$	$(2.3 \pm 0.3 \pm 1.7) \times 10^{-3}$

Table 6: The differential cross sections of $D^{*\pm}$, D^0 (\bar{D}^0), and D^\pm in η bins with $4 < p_T < 100$ GeV; the first uncertainty is statistical, the second is systematic.

$ \eta $ range	$D^{*\pm} d\sigma/d \eta (\mu\text{b})$	$D^0 (\bar{D}^0) d\sigma/d \eta (\mu\text{b})$	$D^\pm d\sigma/d \eta (\mu\text{b})$
0–0.2	$92 \pm 3 \pm 10$	$210 \pm 7 \pm 18$	$87 \pm 3 \pm 11$
0.2–0.4	$96 \pm 11 \pm 11$	$240 \pm 8 \pm 21$	$90 \pm 3 \pm 12$
0.4–0.6	$94 \pm 3 \pm 10$	$243 \pm 9 \pm 21$	$86 \pm 6 \pm 11$
0.6–0.8	$115 \pm 8 \pm 12$	$255 \pm 10 \pm 22$	$93 \pm 7 \pm 12$
0.8–1	$111 \pm 6 \pm 12$	$220 \pm 13 \pm 19$	$102 \pm 5 \pm 19$
1–1.2	$97 \pm 8 \pm 11$	$265 \pm 20 \pm 23$	$107 \pm 5 \pm 19$
1.2–1.4	$106 \pm 14 \pm 12$	$250 \pm 24 \pm 22$	$106 \pm 6 \pm 29$
1.4–1.6	$81 \pm 27 \pm 9$	$265 \pm 27 \pm 24$	$109 \pm 12 \pm 28$
1.6–1.8	$85 \pm 13 \pm 10$	$218 \pm 51 \pm 20$	$112 \pm 11 \pm 24$
1.8–2.1	$70 \pm 9 \pm 17$	$291 \pm 45 \pm 64$	$123 \pm 22 \pm 27$

The differential cross sections for the three mesons as a function of p_T and $|\eta|$ are shown in Figs. 4–6, where the data points (black) are compared to several Monte Carlo event models and theoretical predictions (horizontal lines and bands). The vertical lines on the data points show

the statistical and systematic uncertainties added in quadrature. The cross section values are compared to the predictions of next-to-leading-order plus next-to-leading-logarithmic accuracy (NLO+NLL) calculations by FONLL [10], shown as bands representing the upper and lower limits for a given p_T bin, leading-order plus parton shower (LO+PS) simulations PYTHIA 6 [7] and PYTHIA 8 [8], and NLO+PS calculations from POWHEG [9]. The bottom panel displays the ratio of the FONLL, PYTHIA, and POWHEG predictions to the data points, for which the statistical and total uncertainties are shown by the inner and outer bars, respectively.

The agreement with the different predictions is fair in the wide kinematic range analyzed. None of the MC event generator models describes the data well in all the observed regions. The measurements tend to favor a higher cross section than predicted by FONLL and a lower one than estimated by PYTHIA, although the PYTHIA generator is sensitive to the different parton shower tunes used. The predictions themselves in fact give different estimates of the cross sections and this confirms that the description of charm meson production provided by the models is affected by large uncertainties. Overall, the best description of the data is given by the upper edge of the FONLL uncertainty band. The POWHEG prediction fails at low p_T , for which its input parameters are not optimized.

5.1 Comparison to other experiments

A comparison with the previous results at the LHC provides an overall picture of the charm meson measurements performed at different center-of-mass energies and complementary kinematic regions.

The measurements from the ATLAS experiment [2], although done at $\sqrt{s} = 7$ TeV, are the closest to the one presented in this paper in terms of acceptance and kinematic regime. In Fig. 7 both the ATLAS and the CMS results are shown, compared to the respective FONLL predictions at $\sqrt{s} = 13$ TeV and 7 TeV for both $D^{*\pm}$ (left) and D^\pm (right). Since the ATLAS results include both prompt and nonprompt charm mesons, the corresponding FONLL predictions include both components as well. The results show good agreement in terms of shape, and the comparison between the data points and the theory predictions is very similar for the two experiments. The central value of the FONLL predictions tends to underestimate the data, but the upper edge of the FONLL bands agrees reasonably well.

Comparison with the ALICE results [1] for the three meson cross sections at $\sqrt{s} = 7$ TeV in the range $1 < p_T < 24$ GeV and for the rapidity region $|y| < 0.5$ is shown in Fig. 8. It is important to take into account that the cross section definition by ALICE differs by a factor two from the one by CMS, since in the former the charged conjugates are not included. The same is true for the corresponding FONLL predictions, as well. To provide a relevant comparison, the CMS data are also given for $p_T < 24$ GeV. Both sets of data are consistent with the respective FONLL predictions.

The CMS experiment has also measured the D^0 cross section in pp collisions at $\sqrt{s} = 5.02$ TeV for $|y| < 1$ [6], to allow a comparison with results from heavy-ion collisions at the same energy. Figure 9 shows the 5.02 TeV pp collision measurements in comparison with the FONLL predictions and the corresponding 13 TeV results. Again, in both cases, a similar agreement between data and FONLL predictions is obtained.

The only other measurement performed at $\sqrt{s} = 13$ TeV comes from the LHCb Collaboration [5]. Since the η acceptances of the CMS and LHCb experiments differ, the two measurements are complementary and the results presented in this paper extend the reconstruction to the rapidity region not covered by LHCb. The two measurements are compared in Fig. 10 for the

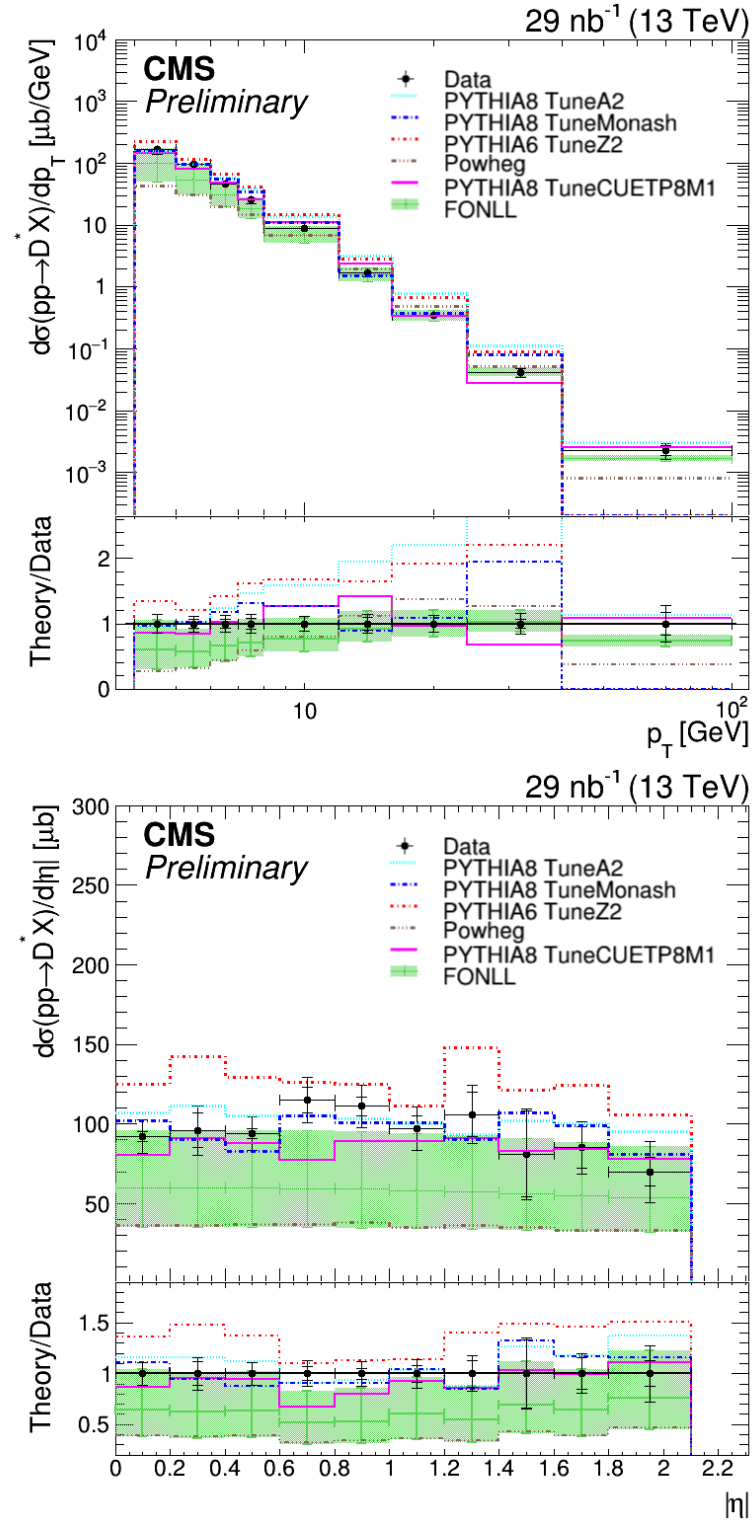


Figure 4: Differential cross sections $d\sigma/dp_T$ (upper) and $d\sigma/d|\eta|$ (lower) for the $D^{*\pm}$ meson. Data points (black) are compared with several MC simulation models and theoretical predictions. The statistical and total uncertainties are reported separated by horizontal bars. On the lower panel of the figures, the ratio of the predictions to the central value of the data is shown.

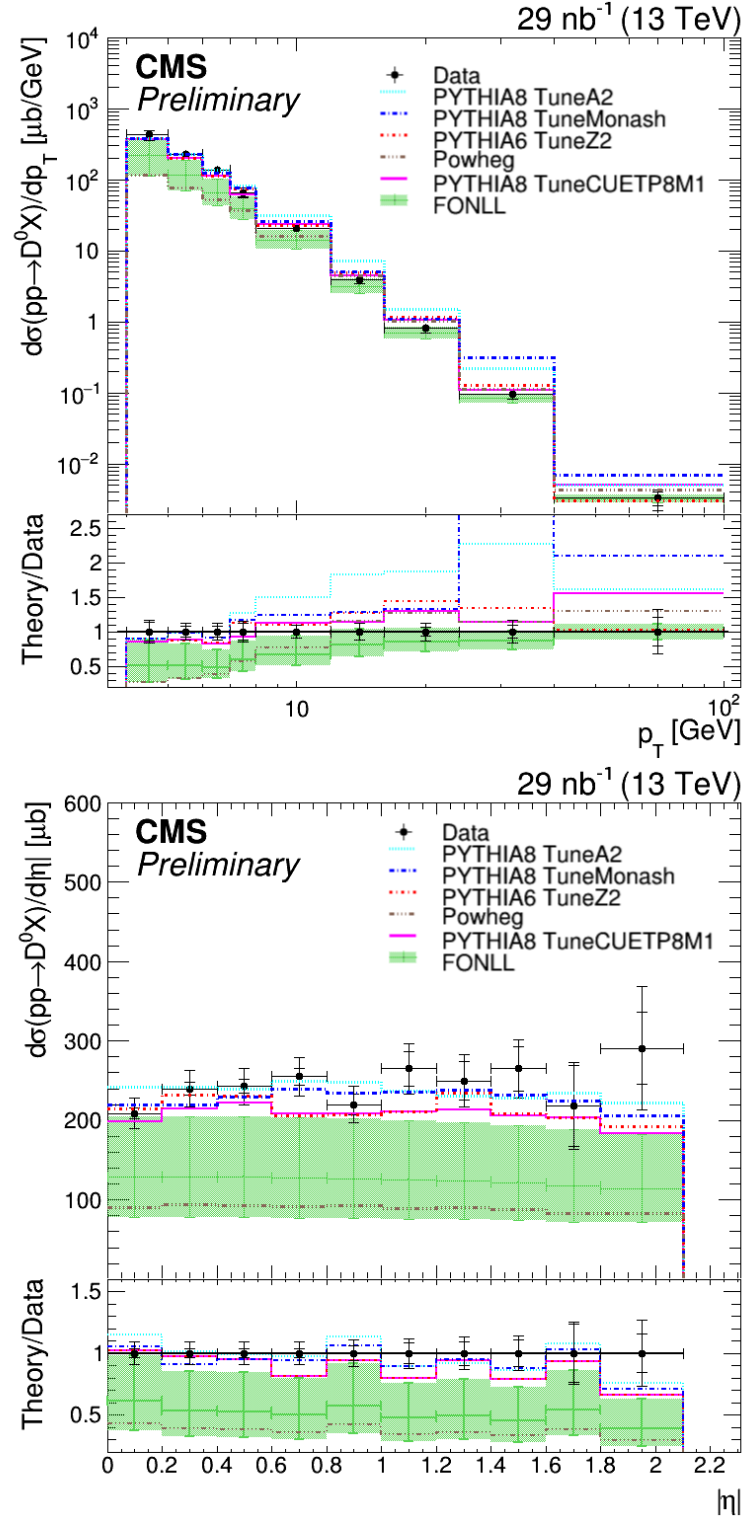


Figure 5: Differential cross section $d\sigma/dp_T$ (upper) and $d\sigma/d|\eta|$ (lower) for the D^0 (\bar{D}^0) meson. Data points (black) are compared with several MC simulation models and theoretical predictions. The statistical and total uncertainties are reported separated by horizontal bars. On the lower panel of the figures, the ratio of the predictions to the central value of the data is shown.

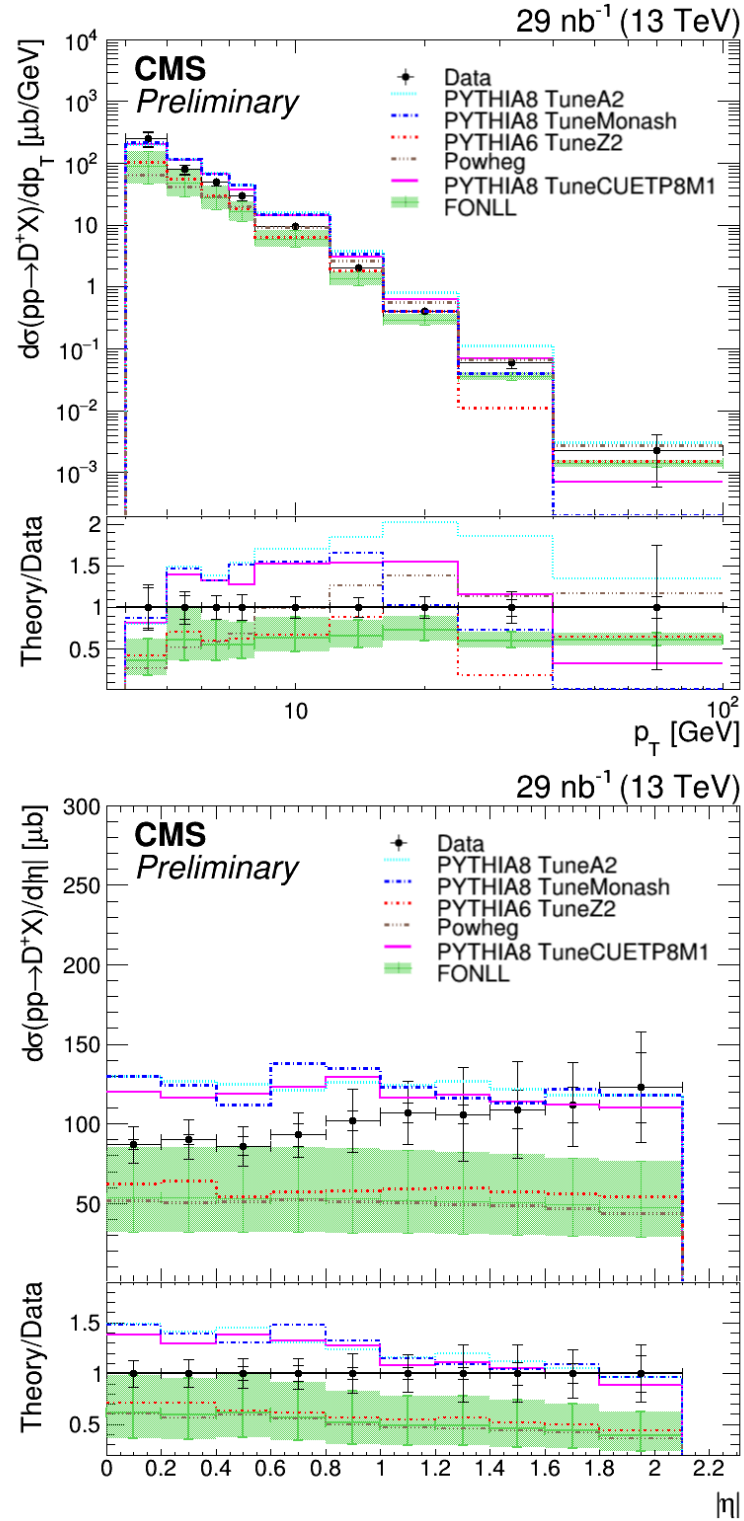


Figure 6: Differential cross section $d\sigma/dp_T$ (upper) and $d\sigma/d|\eta|$ (lower) for the D^\pm meson. Data points (black) are compared with several MC simulation models and theoretical predictions. The statistical and total uncertainties are reported separated by horizontal bars. On the lower panel of the figures, the ratio of the predictions to the central value of the data is shown.

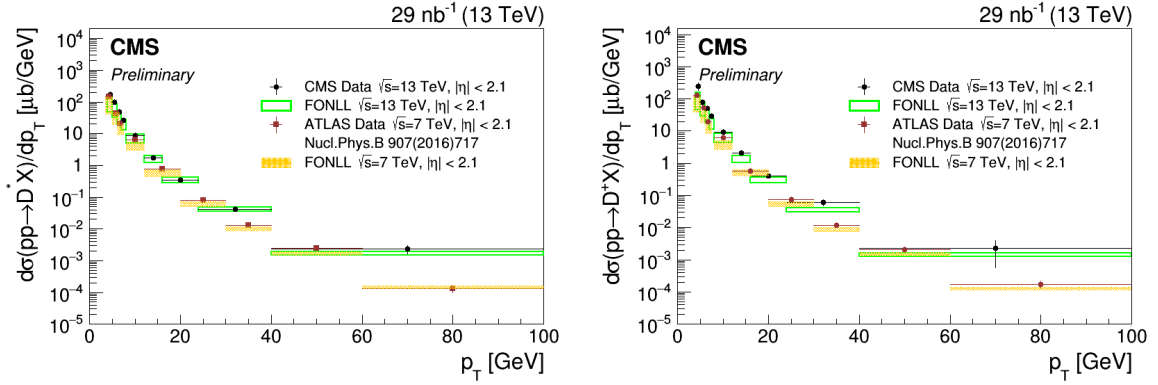


Figure 7: Differential cross section $d\sigma/dp_T$ for the D^{*+} (left) and D^+ (right) mesons, comparing the CMS (circle) and ATLAS (square) data points to the respective FONLL predictions at $\sqrt{s} = 13$ TeV (empty box) and $\sqrt{s} = 7$ TeV (filled box). As the ATLAS data, the corresponding FONLL predictions include both prompt and nonprompt charm meson cross section components.

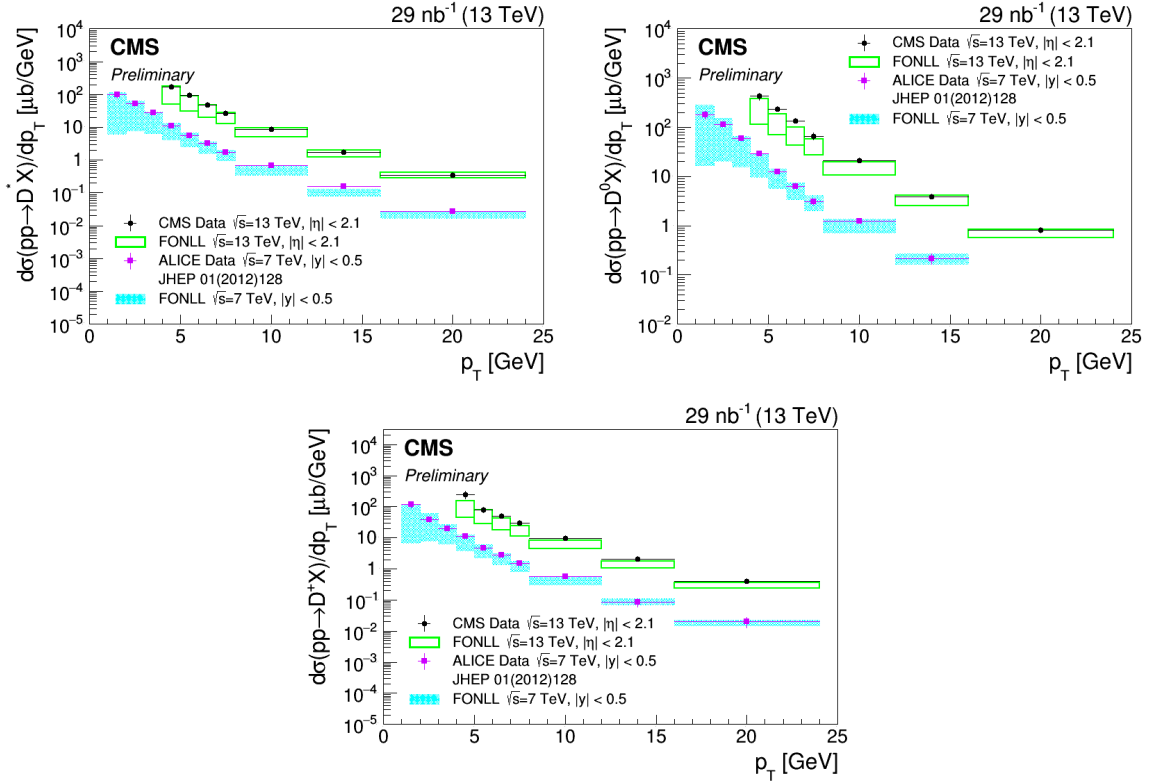


Figure 8: Differential cross section $d\sigma/dp_T$ for the D^{*+} , D^0 and D^+ mesons, comparing the CMS (circle) and ALICE (square) data points to the respective FONLL predictions at $\sqrt{s} = 13$ TeV (empty box) and $\sqrt{s} = 7$ TeV (filled box). The cross section definition by ALICE differs by a factor two from the one by CMS, since in the former the charged conjugates are not included. The same is true for the corresponding FONLL predictions, as well.

LHCb rapidity bin closest to the CMS fiducial region, together with the FONLL predictions. The CMS measurements are shown for $p_T < 16$ GeV to allow a better comparison with the LHCb results. Again, both sets of measurements are in reasonable agreement with the FONLL predictions.

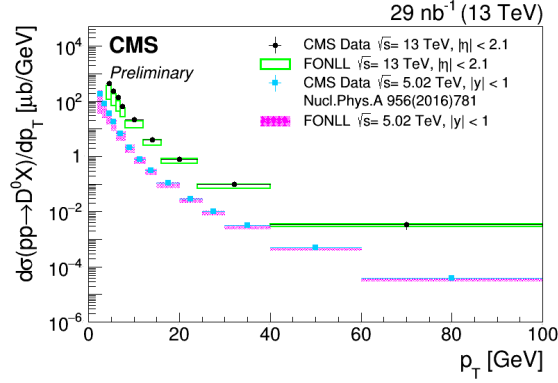


Figure 9: Differential cross section $d\sigma/dp_T$ for the D^0 meson, comparing the CMS measurement at $\sqrt{s} = 13$ TeV (circle) and 5.02 TeV (square) to the respective FONLL predictions at $\sqrt{s} = 13$ TeV (empty box) and $\sqrt{s} = 5.02$ TeV (filled box).

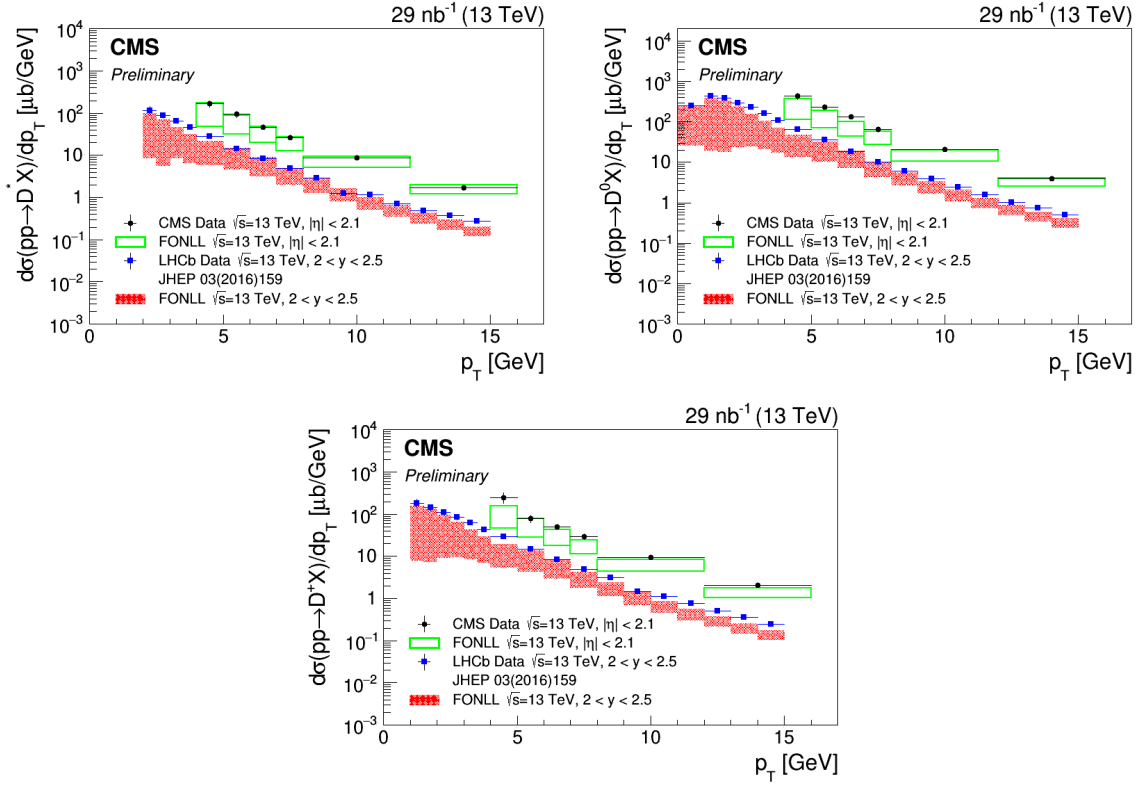


Figure 10: Differential cross section $d\sigma/dp_T$ for the D^{*+} , D^0 and D^+ mesons comparing the CMS measurements at $\sqrt{s} = 13$ TeV (circle) and the LHCb points (square) in the region $2 < y < 2.5$ at $\sqrt{s} = 13$ TeV to the respective FONLL predictions (empty and filled box).

6 Summary

The differential cross sections $d\sigma/dp_T$ and $d\sigma/d|\eta|$ are measured for the charm mesons $D^{*\pm}$, D^0 (\bar{D}^0), and D^\pm in the range $4 < p_T < 100$ GeV and $|\eta| < 2.1$, using data collected by the CMS experiment in proton-proton collisions in 2016 at $\sqrt{s} = 13$ TeV, corresponding to an integrated luminosity of 29 nb^{-1} . The charm mesons were identified in a wide kinematic range with signal invariant mass peaks of high statistical significance. The contamination arising from nonprompt D mesons originating from b hadron decays is removed using Monte Carlo event

simulations. The measured cross section values are compared to different Monte Carlo event generators and theoretical predictions. The agreement with the various models can be considered fair, but no single Monte Carlo simulation or theoretical prediction describes the data well over the entire kinematic range. The measurements tend to favor a higher cross section than predicted by the FONLL calculations [10] and smaller than estimated by the PYTHIA event generators [7, 8]. Overall, the best description is obtained by the upper edge of the FONLL uncertainty band, which can be taken as a reference prediction for background estimations for other processes. This measurement makes a contribution to the understanding of charm meson production in hadronic collisions, which is still dominated by large uncertainties in the present theoretical models.

References

- [1] ALICE Collaboration, “Measurement of charm production at central rapidity in proton-proton collisions at $\sqrt{s} = 7$ TeV”, *JHEP* **01** (2012) 128, doi:10.1007/JHEP01(2012)128, arXiv:1111.1553.
- [2] ATLAS Collaboration, “Measurement of $D^{*\pm}$, D^\pm and D_s^\pm meson production cross sections in pp collisions at $\sqrt{s} = 7$ TeV with the ATLAS detector”, *Nucl. Phys. B* **907** (2016) 717, doi:10.1016/j.nuclphysb.2016.04.032, arXiv:1512.02913.
- [3] LHCb Collaboration, “Measurements of prompt charm production cross-sections in pp collisions at $\sqrt{s} = 5$ TeV”, *JHEP* **06** (2017) 147, doi:10.1007/JHEP06(2017)147, arXiv:1610.02230.
- [4] LHCb Collaboration, “Prompt charm production in pp collisions at $\sqrt{s} = 7$ TeV”, *Nucl. Phys. B* **871** (2013) 1, doi:10.1016/j.nuclphysb.2013.02.010, arXiv:1302.2864.
- [5] LHCb Collaboration, “Measurements of prompt charm production cross-sections in pp collisions at $\sqrt{s} = 13$ TeV”, *JHEP* **03** (2016) 159, doi:10.1007/JHEP03(2016)159, arXiv:1510.01707. [Erratum: JHEP 09, 013 (2016), Erratum: JHEP 05, 074 (2017)].
- [6] CMS Collaboration, “Nuclear modification factor of D^0 mesons in PbPb collisions at $\sqrt{s_{NN}} = 5.02$ TeV”, *Phys. Lett. B* **782** (2018) 474, doi:10.1016/j.physletb.2018.05.074, arXiv:1708.04962.
- [7] T. Sjöstrand, S. Mrenna, and P. Z. Skands, “PYTHIA 6.4 physics and manual”, *JHEP* **05** (2006) 026, doi:10.1088/1126-6708/2006/05/026, arXiv:hep-ph/0603175.
- [8] T. Sjöstrand et al., “An introduction to PYTHIA 8.2”, *Comput. Phys. Commun.* **191** (2015) 159–177, doi:10.1016/j.cpc.2015.01.024, arXiv:1410.3012.
- [9] S. Frixione, P. Nason, and G. Ridolfi, “A positive-weight next-to-leading-order Monte Carlo for heavy flavour hadroproduction”, *JHEP* **09** (2007) 126, doi:10.1088/1126-6708/2007/09/126, arXiv:0707.3088.
- [10] M. Cacciari, M. Greco, and P. Nason, “The p_T spectrum in heavy flavor hadroproduction”, *JHEP* **05** (1998) 007, doi:10.1088/1126-6708/1998/05/007, arXiv:hep-ph/9803400.
- [11] GEANT4 Collaboration, “GEANT4: a simulation toolkit”, *Nucl. Instrum. Meth. A* **506** (2003) 250, doi:10.1016/S0168-9002(03)01368-8.

- [12] D. J. Lange, “The EvtGen particle decay simulation package”, *Nucl. Instrum. Meth. A* **462** (2001) 152, doi:10.1016/S0168-9002(01)00089-4.
- [13] M. Cacciari, G. P. Salam, and G. Soyez, “The anti- k_t jet clustering algorithm”, *JHEP* **04** (2008) 063, doi:10.1088/1126-6708/2008/04/063, arXiv:0802.1189.
- [14] M. Cacciari, G. P. Salam, and G. Soyez, “FastJet user manual”, *Eur. Phys. J. C* **72** (2012) 1896, doi:10.1140/epjc/s10052-012-1896-2, arXiv:1111.6097.
- [15] Particle Data Group Collaboration, “Review of particle physics”, *Phys. Rev. D* **98** (2018) 030001, doi:10.1103/PhysRevD.98.030001.
- [16] CMS Collaboration, “Measurement of Tracking Efficiency”, CMS Physics Analysis Summary CMS-PAS-TRK-10-002, CERN, 2010.
- [17] CMS Collaboration, “Tracking POG results for pion efficiency with the D^* meson using data from 2016 and 2017”, Technical Report CMS-DP-2018-050, CERN, 2018.
- [18] M. J. Oreglia, “A study of the reactions $\psi' \rightarrow \gamma\gamma\psi$ ”, *SLAC-R-236* (1980).
- [19] J. E. Gaiser, “Charmonium spectroscopy from radiative decays of the J/ψ and ψ'' ”, *SLAC-R-255* (1982).
- [20] CMS Collaboration, “CMS Luminosity Measurements for the 2016 data taking period”, CMS Physics Analysis Summary CMS-PAS-LUM-17-001, CERN, 2017.